Corrosion Science 199 (2022) 110152

Contents lists available at ScienceDirect

Corrosion Science

journal homepage: www.elsevier.com/locate/corsci

Investigation of the fireside corrosion of a new wrought Ni-Fe-Cr-based alloy in advanced ultra-supercritical steam boilers

Jiali Wang [a], Jiankun Zhuo [a,*], Qiang Yao [a,b]

[a] Key Laboratory for Thermal Science and Power Engineering of Ministry of Education, Department of Energy and Power Engineering, Tsinghua University, Beijing 100084, China
[b] School of Electric Engineering, Xinjiang University, Urumqi 830047, China

ARTICLE INFO

Keywords:
A. Ni-Fe-Cr based superalloy
B. optical examination
C. Fireside corrosion

ABSTRACT

The gas-phase and coal ash-related fireside corrosion behavior of a new type of Ni-Fe-Cr based superalloy GH984G and two other contrast alloys were investigated for its application under advanced ultra-supercritical (A-USC) conditions. Results showed that the oxidation activation energy of the three alloys at 600–780 °C in the flue gas environment can be ranked from large to small: C-HRA-1>GH984G>Alloy 625. In the coal ash environment, GH984G and C-HRA-1 exhibited satisfactory corrosion resistance, while Alloy 625 had weaker corrosion resistance due to the presence of molybdenum. The corrosion mechanism of GH984G and the influence of constituent elements were elucidated.

1. Introduction

In recent years, the reduction of pollutant emissions and CO_2 in fossil-fuel thermal power plants has been increasingly studied and extensively discussed. Efficiency improvement will play an important role in CO_2 reduction. Compared with traditional fossil fuel-fired boilers, advanced ultra-supercritical technology operating at 760 °C and 35 Mpa has higher thermal efficiency (over 50%) and low CO_2 emissions (40–50% less CO_2) [1,2]. Therefore, this technology is promising for future CO_2 emission reduction in thermal power plants.

However, considering the harsher working conditions of heat-transfer components, the advanced ferritic and austenitic stainless steels currently used will no longer be capable of meeting the new stringent material standards [3,4]. One of the critical limiting factors for increasing steam temperature and pressure in future advanced ultra-supercritical power plants is the performance of structural materials. Advanced Ni-based superalloys are promising alloys for A-USC applications with outstanding creep rupture strength and resistance to high-temperature corrosion [5,6]. The THERMIE AD700 project requires candidate alloys with a superior creep rupture strength of 100 Mpa/10^5 h and a corrosion resistance of $\leq$ 2 mm cross-section loss in 2 $\times$ 10^5 h at 750 °C [1,7,8].

However, the high cost of nickel and cobalt affects the promotion of nickel-based alloys in large components. From the perspective of alleviating the abovementioned problems to develop alloys, the addition of iron to the alloys will reduce costs and improve workability. Recently, some novel Ni-Fe-Cr-based alloys have not only exhibited promising mechanical properties but have also possessed competitive advantages, such as high thermal conductivity, superior processing properties and cost-effective characteristics. Some of them have been increasingly studied as interesting alternatives, such as SINM (Ni-30Fe-17.5Cr-1.8Ti-1.6Al-1.2Nb-0.5Mo) [9], HR6W (Ni-23Cr-24Fe-6W-Ti, wt%) [10], and the newly developed Ni-Fe-Cr-based alloy (Ni-30Fe-20Cr-2.2Ti-2Al-(0–0.3)Y, wt%) [11,12]. These Ni-Fe-Cr-based alloys form a multi-layered scale on the alloy surface, and exhibited obviously coal ash-related corrosion. The fireside corrosion of Ni-Fe-Cr-based alloys varied with composition, and the oxidation mechanism is not yet completely clear. A new Ni-Fe-Cr-based wrought superalloy GH984G has been specially developed by the Metal Research Institute, Chinese Academy of Sciences [13,14]. Research has shown that GH984G exhibits satisfactory microstructural stability and mechanical properties in the range of 600–800 °C [15,16]; furthermore, GH984G has excellent steam-side oxidation resistance at 700 °C [17]. Fireside corrosion might cause the failure of heat-transfer components, so this corrosion has become one of the key issues for the application of GH984G in aggressive combustion environments [18]. Recently, Liu et al. [19,20] studied that corrosion behaviors of GH984G in synthetic coal ash and flue gas environment at 700 °C. However, the oxidation rate constant and the oxidation activation of GH984G in flue gas environment were not studied. The coal ash deposit is prepared using the synthetic mixture of

* Corresponding author.

https://doi.org/10.1016/j.corsci.2022.110152
Received 20 May 2021; Received in revised form 29 January 2022; Accepted 3 February 2022
Available online 8 February 2022

alkali sulphates and Fe_2O_3 instead of the real boiler fly ash deposit in the coal ash-related corrosion. Therefore, fireside corrosion of GH984G needs to be further studied.

It is well known that fireside corrosion is the combined effect of gas-phase corrosion and coal ash-related corrosion [18]. Gas-phase corrosion experiments are conducted in a tube furnace reactor from 600° to 780°C for 1000 h in simulated flue gas environments. However, it is difficult to reveal actual the coal ash-related corrosion status of an operating boiler in laboratory tests. Most investigations either only focus on the influence of the flue gas composition or use traditional sediment recoating techniques to estimate coal ash corrosion, thereby neglecting the delamination of ash deposits and interaction with alloys [18,21]. In this study, an initial ash deposit layer is formed in a lab-scale entrained pulverized coal furnace and contains submicron particles and low-melting inorganic matter. The deposited ash is expected to allow the study of the coal ash-related corrosion behaviours of selected materials. The corrosion process is determined using the traditional weight change method and dimensional metrology of sample cross-sections. The morphological characteristics of the corrosion products are studied utilizing optical examination. The influence of constituent elements and the corrosion mechanism of GH984G are elucidated. Finally, reliable data and recommendations for the proposed tubing alloys designed for A-USC boilers is provided.

2. Experimental procedure

2.1. Corrosion tests

Three dedicated alloys with different compositions (see Table 1) applied for A-USC boiler were selected for fireside corrosion experiments, namely, GH984G, C-HRA-1 and Alloy 625. A new Ni-Fe-Cr-based wrought superalloy GH984G contains chromium and molybdenum for solid solution strengthening, 3.47% of sum of aluminium, titanium and niobium for precipitation strengthening. GH984G is specially developed on the basis of a GH984 by increasing chromium content, reducing Ti/Al radio , decreasing iron content and adding a trace of boron to improve thermal stability and grain boundary strength [13–17]. C-HRA-1 is a Ni-Co-Cr-based material developed by Baoshan Iron & Steel Co., Ltd, and is developed based on Nimonic 263 for improving its corrosion resistance [22,23]. The application of C-HRA-1 in the A-USC boiler is similar to that of Inconel 740H and 617B; thus, C-HRA-1 has been recognized as a promising candidate for A-USC. Alloy 625, with its high molybdenum content, is well known for its application in various industries.

The test specimens were manufactured with an appropriate dimension of approximately 20 mm × 10 mm× 3 mm by electrical discharge method. The surfaces were manually ground by 800-grit SiC paper. The specimens were thoroughly degreased in acetone, then were washed in deionized water in ultrasonic cleaners. The specimens were finally dried and weighed.

The long-term laboratory exposures were carried out in an electrically heated furnace equipped with a quartz chamber, and a quartz boat with the specimens was placed in the constant temperature zone according to the criterion of ISO/TC 156 [24]. Fig. 1 shows the schematic diagram of the experimental system.

The experimental parameters were set to simulate the flue gas composition and wall temperatures of the superheater and reheater sections of the A-USC boiler. The simulated flue gas mixture was composed of 79.4% N_2, 4.5% O_2, 16% CO_2, and 0.1% SO_2 (vol%) at a flow rate of approximately 20 ml/min. The gas was fed through a platinum catalyst screen to maintain the SO_2/SO_3 equilibrium in the mixed gas. The exhaust gas was first absorbed by a saturated sodium hydroxide solution before being discharged into the atmosphere. The temperatures were set at 600, 680 and 780 °C to investigate the performance of the selected alloys at different wall temperatures experienced by A-USC boiler heat exchangers.

Fireside corrosion is mainly related to ash deposits on the surface of boiler tubes. The inner layer of deposited ash on the heat exchanger surface is almost completely composed of submicron particles and low-melting inorganic matter (such as Na, K, Fe-containing compounds or sulfides) [25]. Ash deposition on the specimens was carried out in a lab-scale entrained pulverized coal furnace to 10 mg/cm^2, and then the specimens were placed in an isothermal tube furnace at 780 °C for up to 1000 h. Fig. 2 illustrates a schematic diagram of the combustion and ash deposition system. The system mainly consisted of a scraper feeder, a two-stage air supply system (the excess air ratio was set to 1.2 to ensure the burnout rate of pulverized coal), a SiC-tube reactor, and a home-made air-cooled sampler. The ash deposition probe in the air-cooled sampler was loaded with alloy specimens on its surface and was placed at the outlet of the furnace. A type K thermocouple was installed between the alloy specimens and the surface of the air-cooling chamber. The temperature signal was transferred to the air-cooling flow controller to keep the specimen temperature at 780 °C by adjusting the gas flow through the air-cooling chamber.

In the combustion tests, Zhundong lignite feedstock, which is characterized by its high sodium and sulfur contents, was selected to be fed due to the sensitivity of alloy corrosion to alkali metals and sulfur [25,26]. The proximate and ultimate analysis and coal ash composition of Zhundong lignite are shown in Table 2. The composition and microstructure of the ash deposit was analysed by inductively coupled plasma-mass spectrometry (ICP-MS, Thermo X Series) and electron probe microanalysis (EPMA, JXA-8230), respectively. To facilitate the description of the specimens, the specimens treated by ash deposition are labelled pre-exposure, and the uncoated samples are marked as deposit-free.

The progress of the corrosion process was determined using traditional weight changes and scale thickness (if any, the spalling of scales). Three parallel specimens were used to achieve experimental repeatability. After completing the long-term deposited ash corrosion experiments, the pre-exposure samples were cleaned and placed in Bakelite at 160 °C and 30 Mpa by a metallographic inlaying machine. When fully solidified, the inlaid samples were cut, ground, and polished prior to analysis. The corrosion products presented in samples surface were characterized by X-ray diffraction (XRD, Bruker D8 Advance) with a Cu tube producing K-α1 X-Rays of 1.54 Å. The diffraction patterns were recorded in an angular interval of 10–90°. Scanning electron microscopy (SEM) and energy dispersive X-ray spectroscopy (EDS) were utilized to obtain the morphologies and elemental compositions of the corrosion layer on the specimens. The SEM-EDS analysis was performed by Zeiss Merlin at an acceleration voltage of 200 kV. The samples were carbon sputtered before the SEM observations.

Table 1
Composition of the tested materials (wt%).

Material	C	Nb	Ti	Al	Co	Cr	Mo	Fe	Ni	Others
GH984G	0.044	1.22	1.3	0.95	–	20.9	2.24	20.71	Bal.[a]	0.004 B
C-HRA-1	0.022	1.43	1.29	1.52	20.7	24.9	0.3	0.07	Bal.	0.02 Mn;0.06 Si
Alloy 625	0.05	3.7	0.2	0.2	–	21.5	8.9	2.6	Bal.	0.3 Mn;0.3 Si

[a] Balance.

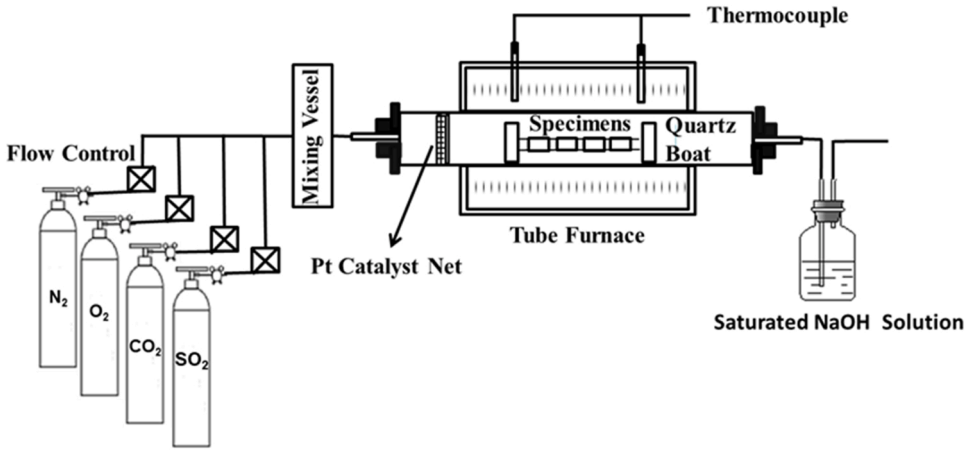

Fig. 1. Schematic diagram of the corrosion experiment system.

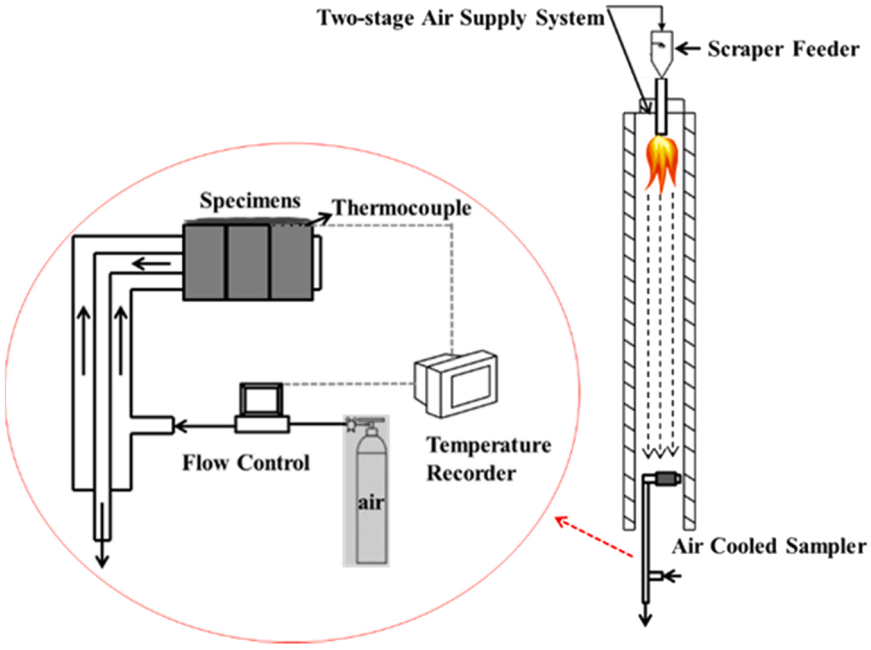

Fig. 2. Schematic diagram of the combustion and ash deposition system.

Table 2
Composition of the coal ash deposit in the combustion tests (wt%).

Ultimate analysis	Dry and ash-free basis	Ash composition	Ash
C	71.52	SiO_2	28.5
H	3.29	Al_2O_3	4.6
N	0.75	Fe_2O_3	6.3
S	0.53	CaO	32.7
O	23.83	MgO	4.1
Cl	0.08	SO_3	15.4
		K_2O	0.7
		Na_2O	7.7

2.2. Computational approach

The influence of introduced by iron on the diffusion of chromium in close-packed face-centered-cubic (fcc) Ni lattice can be analysed by first-principles density functional theory (DFT) calculations. The relevant energetics are computed in the Cambridge Serial Total Energy Package (CASTEP) program [27] with generalized gradient approximation Perdew-Burke-Ernzerhof functional (GGA-PBE) [28]. The fcc Ni lattice is represented by a 3 × 3 × 3 supercell including 108 atoms. The Brillouin zone k-point grid is set to 3 × 3 × 3 with a 310 eV energy cut-off of the plane waves. The convergence parameters are set as following: 10^{-5} eV/atom for total energy per atom, 0.03 eV/Å for maximum ionic force, 0.05 Gpa for maximum stress in the unit cell, and 0.001 Å for maximum atomic displacement.

3. Results

3.1. Corrosion kinetics on the uncoated samples

The relationship between the mass change and exposure time of the selected alloys between 600 and 780 °C is shown in Fig. 3a-c. The mass of all alloys also increases with increasing time, and the increase in mass depends on the chemical composition of the alloy. Furthermore, all the alloys witness quasi-parabolic growth over time, which is observed in the oxidation of various alloys [29–31]. The quasi-parabolic growth follows the Wagner law and can be expressed in Eq. (1):

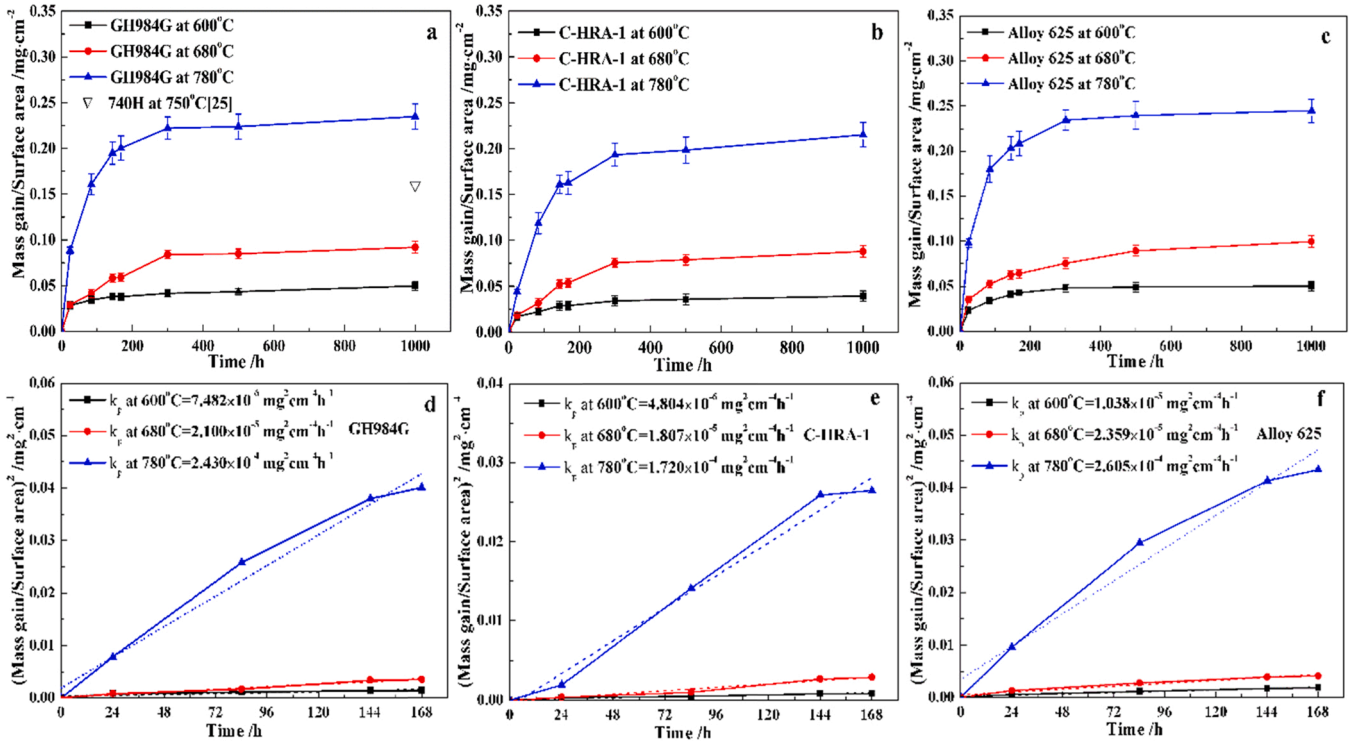

Fig. 3. (a-c) Mass gain per surface area vs. exposure time curves and (d-f) parabolic plots of the square of mass gain per surface area vs. exposure time at 600, 680 and 780 °C for 1000 h on uncoated GH984G, C-HRA-1, and Alloy 625.

$$(\frac{\Delta W}{A})^2 = k_p t \quad (1)$$

where (ΔW/A) represents the weight change per surface area (mg/cm^2), t is the exposure time (h), kp is the parabolic rate constant (mg^2 cm^{-4} h^{-1}). The initial rapid from 0 to 168 h and then almost unchanged after 168 h growth pattern indicates the formation of protective barriers on the surface in 168 h. Since the formation of protective barriers on the surface restricts the inward and outward diffusion of active ions, and the oxidation process enters a stable stage after the oxide scale reaches a certain thickness. The kp values of the three tested alloys can be obtained from the slope of the fitting between $(\Delta W/A)^2$ and t in the first 168 h exposure time. The kp values are shown in Fig. 3d-f and Table 3. The kp values are related to the oxidation rates of alloys. The kp values of the three alloys at 600–780 °C are ranked from large to small: Alloy 625 >GH984G>C-HRA-1. This result indicates that the oxidation rate of GH984G is between those of C-HRA-1 and Alloy 625 in the deposit-free case. In Fig. 3a, the corrosion rates of GH984G are compared with the corresponding value obtained with Inconel 740H at 750 °C for 1000 h by deBarbadillo [29]. The results show that the corrosion rate of GH984G is comparable to that of Inconel 740H in a flue gas environment.

The kp values of GH984G at 600, 680, and 780 °C are 7.482×10^{-6}, 2.100×10^{-5}, and 2.430×10^{-4} mg^{2}cm^{-4}h^{-1}, respectively. The kp values increase with increasing temperature, suggesting that oxidation occurs more easily at elevated temperatures. The increase in mass of the alloys is also affected by temperature. When the temperature is increased from 600° to 680°C, the mass increases slightly. However, a significant acceleration of the increase in mass is measured at 780 °C.

Table 3
Parabolic rate constant values (kp) of the three alloys (mg^2 cm^{-4} h^{-1}).

Material	600 °C	680 °C	780 °C
GH984G	7.482×10^{-6}	2.100×10^{-5}	2.430×10^{-4}
C-HRA-1	4.804×10^{-6}	1.807×10^{-5}	1.720×10^{-4}
Alloy 625	1.038×10^{-5}	2.359×10^{-5}	2.605×10^{-4}

After 1000 h of exposure, the corrosion characteristics in terms of the average scale thickness for the tested alloys have a good correlation with the increase in mass, as illustrated in Fig. 4. It is imperative to declare that scaling thickness is mainly proposed to represent the thickness of the external Cr_2O_3 scale in this study. The results show that the scale thicknesses of the tested alloys increase with increasing temperature. These three alloys exhibit scale thicknesses of 0.3 μm at 600 °C after 1000 h of exposure. At 680 °C, the scaling rates of all alloys increase up to approximately 0.6 μm/1000 h. At 780 °C, the scaling rates for the three tested alloys show a dramatic increase. After 1000 h of exposure, the scale thicknesses for GH984G, C-HRA-1 and Alloy 625 are 1.79 μm, 1.58 μm and 1.83 μm, respectively. The scale thickness of GH984G lies

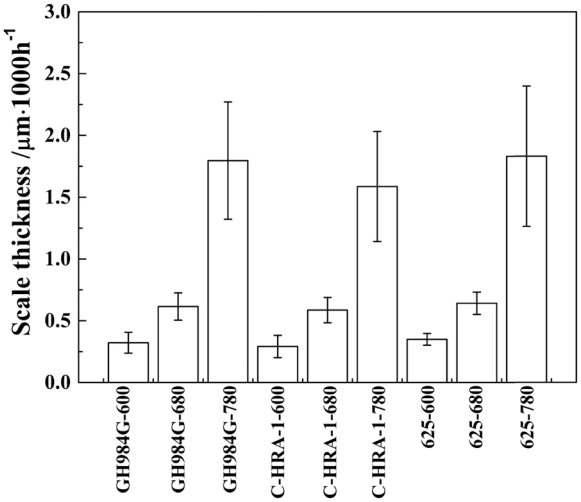

Fig. 4. Scale thickness after exposure for 1000 h at 600, 680 and 780 °C on uncoated GH984G, C-HRA-1, and Alloy 625.

between those of C-HRA-1 and Alloy 625. These results indicate that the scale thickness is positively related to the oxidation rate constant.

3.2. Characterization of the corrosion products on the uncoated samples

The cross-sectional morphology and composition of GH984G at 600, 680 and 780 °C after 1000 h of exposure are shown in Figs. 5–7. Similar to the weight increase in Fig. 3, the scale thickness increases with increasing temperature after 1000 h of exposure. At 600 and 680 °C, the oxide scales are thin, consisting of an external oxidation layer that is dominated by chromium and an inner oxidation layer rich in aluminium; moreover, there is no obvious iron oxide layer, as shown in Figs. 5 and 6.

When the temperature is increased to 780 °C, the GH984G specimen generates thicker and more uneven oxide scales, which exceed 3 μm (Fig. 7). The oxide scales are mainly composed of two distinct types of oxides based on their morphology: a continuous external layer of a chromium-dominated oxide with a small amount of titanium and a discontinuous internal layer of an aluminium-rich oxide in the matrix. The thin external Cr_2O_3 layer suppresses the activity of oxygen at the metal-scale interface, where aluminium and titanium can form stable oxides because of their low oxidation activation energy [32]. We can see that aluminium generates discontinuous root-like internal oxides at the outer oxide layer/matrix interface, which are formed by the counter current of oxygen and aluminium at the grain boundaries [33]. Titanium tends to form a thin continuous layer with irregular titanium-rich nodules close to the alloy surface due to its high outward diffusion rate [32]. However, other constituent elements, such as iron, nickel and niobium, are not detected anywhere in the oxide layer.

Furthermore, an intriguing issue is the evolution of the oxide layer characteristics. Fig. 8 shows the cross-sectional micrographs and elemental distribution of GH984G after exposure for 168 h at 780 °C. Note that GH984G cannot form a continuous and dense structure of oxide scales after 168 h of exposure, while a relative aggregation of iron- and nickel-rich oxide layers can be observed on the surface (indicated by red dashed line). When the exposure duration is increased to 1000 h, the chromium-rich oxide layer thickens and compacts; moreover, the iron-rich oxide layer disappears (Fig. 7).

The XRD patterns of the surface scales of GH984G after 1000 h of exposure at 600, 680 and 780 °C are shown in Fig. 9. The surface scales are identified as the main substrate, and a small amount of Cr_2O_3 and $NiFeCrO_4$ is observed, indicating that the oxide layers generated on the alloy surface are thin. This result is confirmed by the elemental mapping results. Additionally, the diffraction patterns are almost the same at different temperatures; additionally, the oxide diffraction peaks are slightly stronger at 780 °C. These results show that the oxidation process is accelerated with increasing temperature.

After exposure at 780 °C for 1000 h, the oxide scale structure of C-HRA-1 is similar to that of GH984G, consisting of an outer Cr_2O_3-dominated layer and an inner aluminium-rich oxide layer (Fig. 10). In the case of Alloy 625, only the external layer with an abundance of chromium oxide is detected (Fig. 11).

3.3. Deposit-induced corrosion

The cross-sectional morphology and composition of the initial ash deposit formed on the specimen surface in the combustion experiments with Zhundong lignite were analysed by EPMA, and the results are shown in Fig. 12. The initial deposit layer is mainly classified as outer and inner layers: the outer layer consists of irregular agglomerated particles with sizes larger than 10 μm. The inner layer, composed of fine particles rich in calcium, sulfur, silicon, sodium, etc., is observed to adhere to the specimen surface due to condensation and thermophoresis [34], which tends to increase the sulfur activity at the scale/flue gas interface with the tested alloys [35,36]. The corrosive alkali sulphates were not obviously observed to form in initial ash deposit layer in Fig. 12. In addition, based on the work of Corey and Reid [25,26], at least 2.5×10^{-4} atm SO_3 is required to stabilize the liquid melt of alkali-iron trisulfates at 593 ℃. Furthermore, with increasing temperature, the equilibrium amount of SO_3 in the gas decreases, and a higher level of SO_3 is required to stabilize low-melting-point eutectics. Therefore, there was not enough SO_3 (2.144×10^{-4} atm in this experiment) in the present experimental environment to foster the formation of low-melting-point compounds.

Fig. 13 shows the cross-sectional micrographs and elemental mapping of GH984G after 1000 h of exposure to coal ash deposits at 780 °C. Although the coal ash deposit contains a certain amount of sodium and sulfur known for their significant corrosive effects in low-temperature hot corrosion [25,26], GH984G has barely been attacked by this type of corrosion, and no signs of sulfur are detected in GH984G, which indicates its superior capability to resist deposit-induced corrosion. GH984G generates oxide scales exhibiting a double-layered structure similar to that in the deposit-free case, and the continuous external Cr_2O_3 scale can limit the inward diffusion of oxygen and sulfur, thereby resisting sulfidation [33,35]. The Cr_2O_3 scale thickness of 1.76 μm after 1000 h of pre-exposure is thinner than those on the uncoated samples (1.79 μm/1000 h).

Fig. 14 presents a comparison of the XRD patterns for pre-exposure and uncoated samples of GH984G at 780 °C. The diffraction patterns

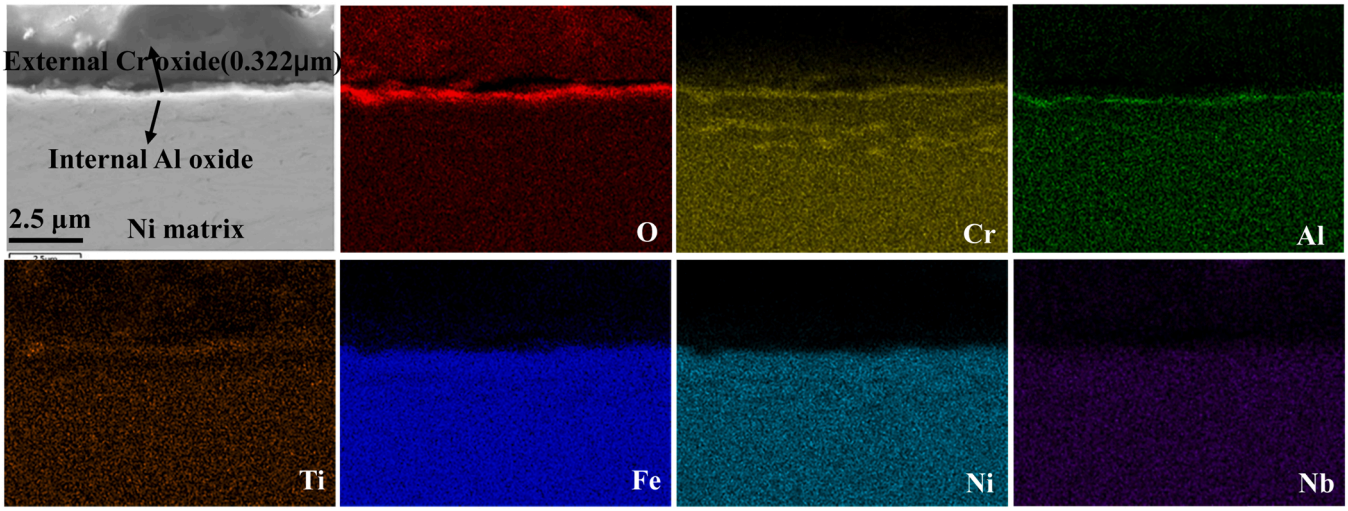

Fig. 5. EDS mapping results of the uncoated GH984G samples after exposure for 1000 h at 600 °C.

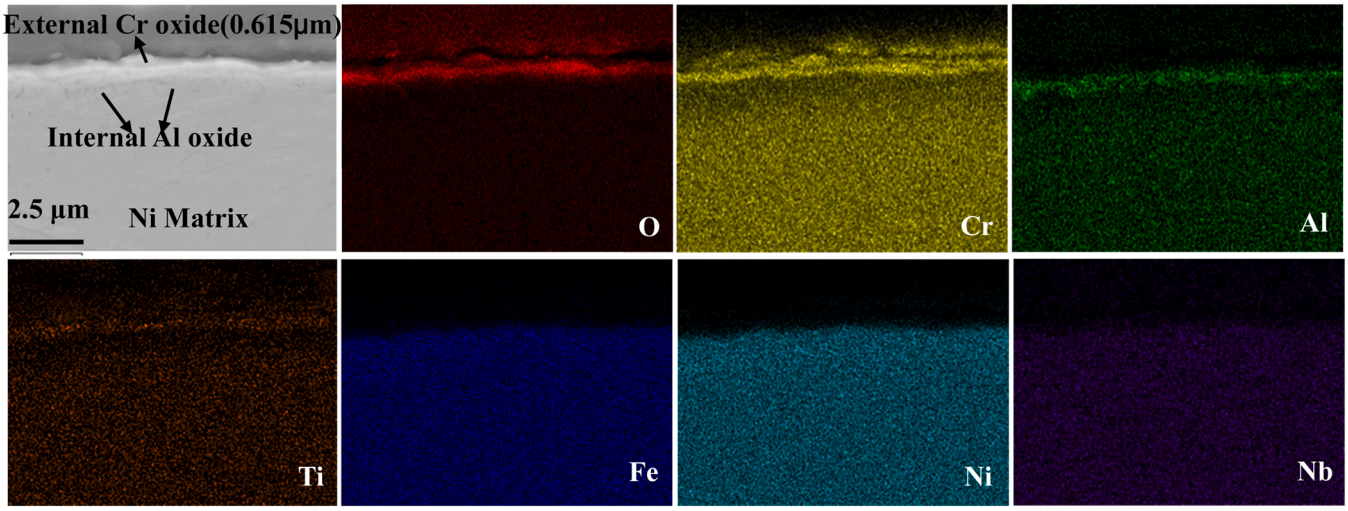

Fig. 6. EDS mapping results of the uncoated GH984G samples after exposure for 1000 h at 680 °C.

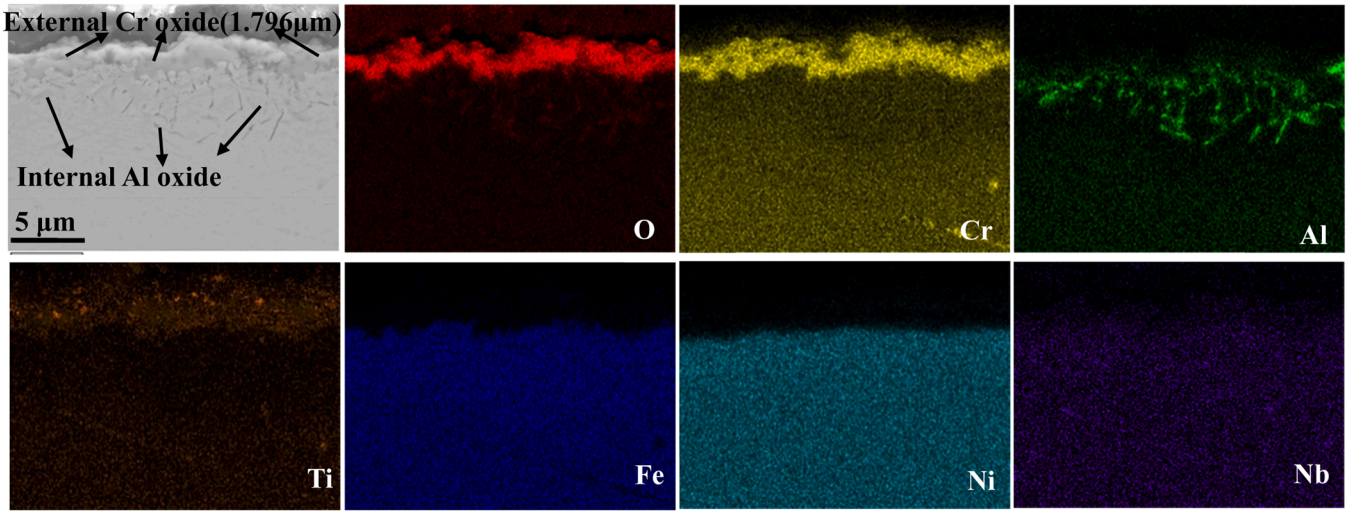

Fig. 7. EDS mapping results of the uncoated GH984G samples after exposure for 1000 h at 780 °C.

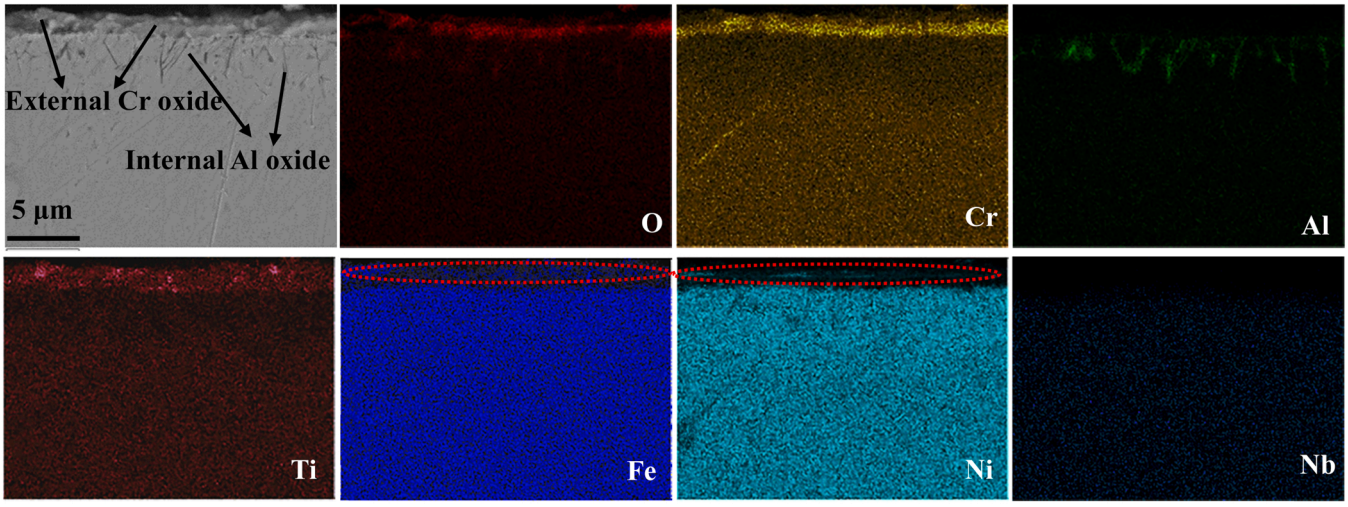

Fig. 8. EDS mapping results of the uncoated GH984G samples after exposure for 168 h at 780 °C.

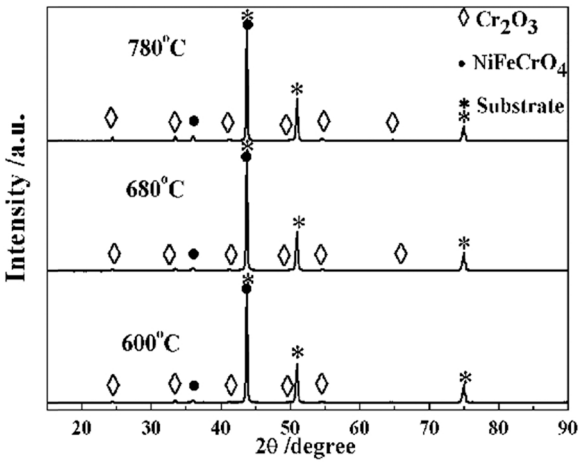

Fig. 9. XRD patterns of the surface scales on GH984G after exposure to the gas environment for 1000 h at 600 °C, 680 °C and 780 °C.

of the surface scales appear to be similar, but the oxide diffraction peaks of uncoated samples are slightly stronger than those of pre-exposure samples. It can be inferred that in the presence of ash deposits, oxide scales formed on the specimens become thinner than those on the uncoated samples. Therefore, it is proposed that the coal ash deposit can be used to a certain extent as an insulation barrier against the oxidation of GH984G in high-temperature flue gas.

Similarly, C-HRA-1 also forms a protective external Cr_2O_3 layer and exhibits barely any signs of sulfur corrosion. Alloy 625 reveals obvious signs of interaction with sulfur. Alloy 625 forms internal sulfides at the scale/matrix interface as well as in the matrix. Sulfur is detected below the multilayer external scale and is rich in molybdenum, chromium and niobium (Fig. 15). It is imperative to declare that since there is overlap between the K-peak of S and the L-peak of Mo, the S and Mo mapping profiles in Fig. 14 are considered to represent the Mo + S distribution. Alloy 625 with 21.5% chromium suffers severe sulfidation attack due to the undesirable presence of molybdenum. Brewer [37] and Gagliano [38] et al. explained that a high molybdenum concentration was conducive to the formation of molybdenum sulfide when sulfur activity was sufficiently high. Furthermore, the internal sulfides deteriorate the

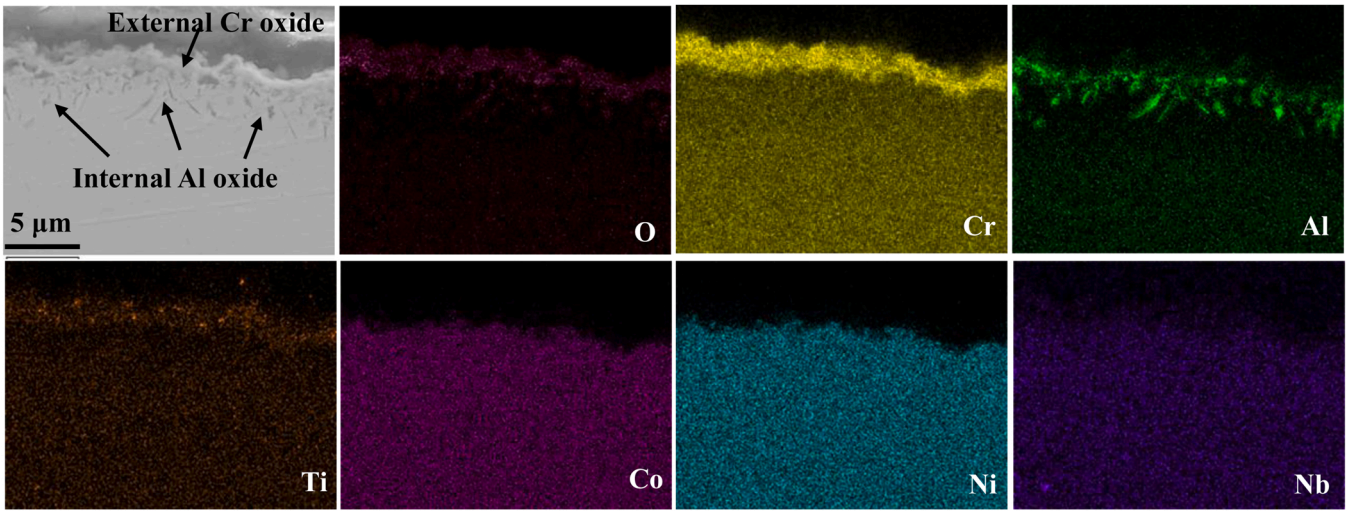

Fig. 10. EDS mapping results of the uncoated C-HRA-1 samples after exposure for 1000 h at 780 °C.

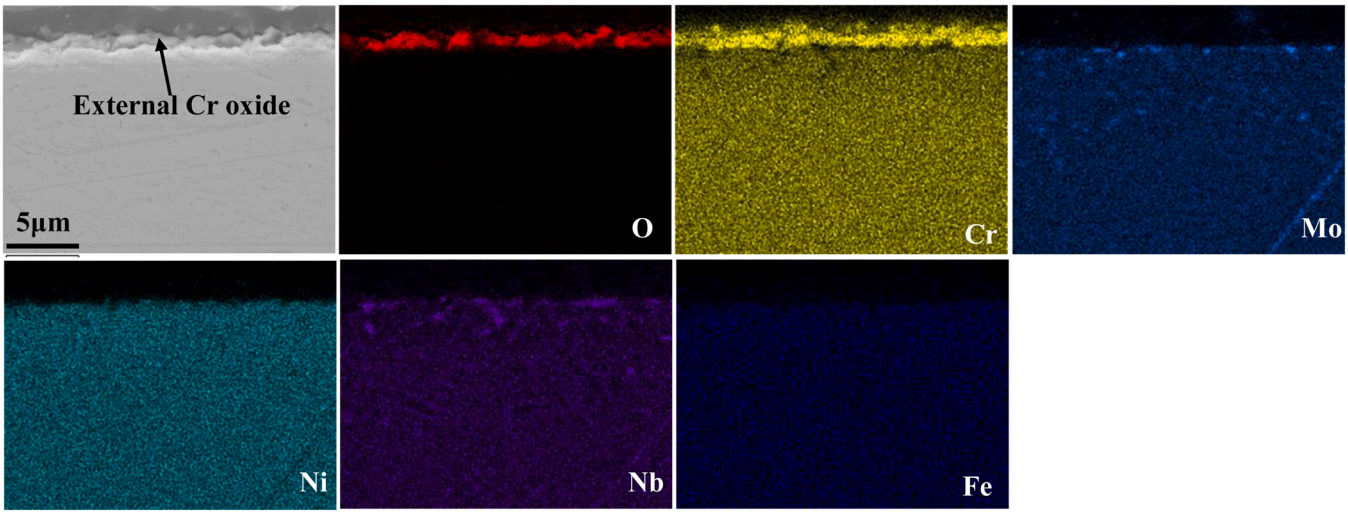

Fig. 11. EDS mapping results of the uncoated Alloy 625 samples after exposure for 1000 h at 780 °C.

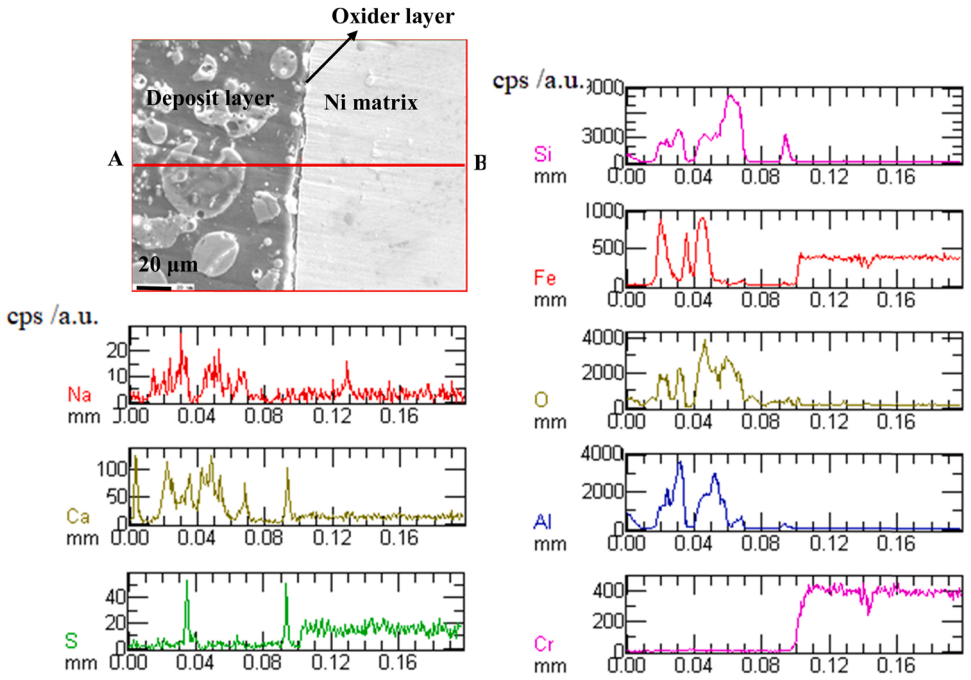

Fig. 12. Cross-sectional morphologies of the initial ash deposit and composition analysis from A to B by EMPA.

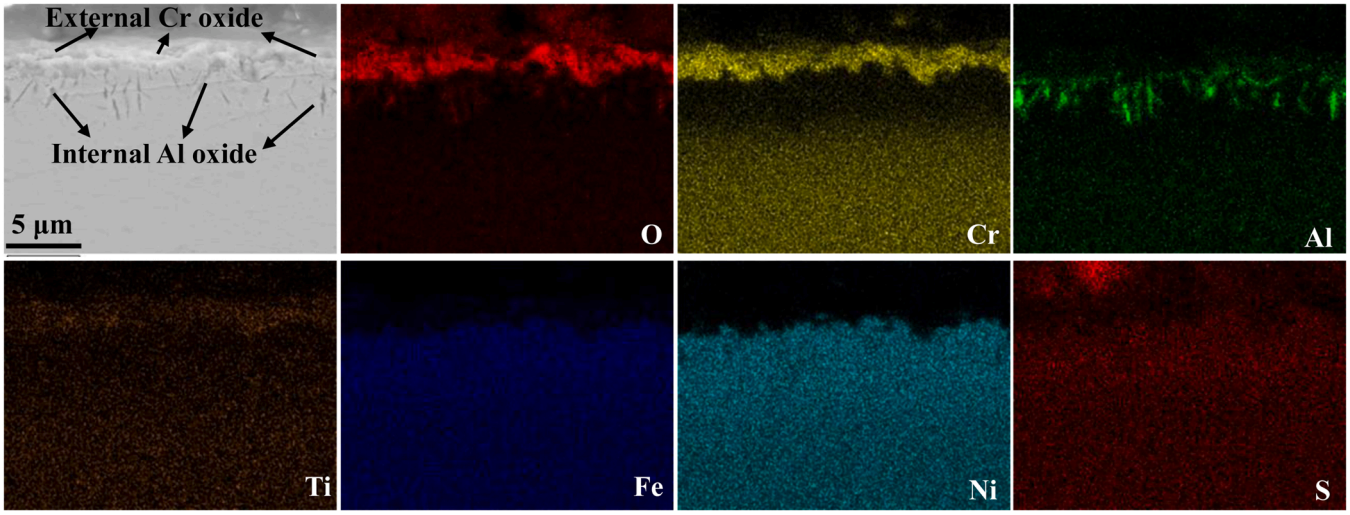

Fig. 13. EDS mapping results of the pre-exposure GH984G samples after exposure for 1000 h at 780 °C.

capability of the Cr_2O_3 scale to resist further corrosion.

As discussed above, in the coal ash environment, GH984G and C-HRA-1 exhibited satisfactory corrosion resistance, while Alloy 625 had weaker corrosion resistance due to the presence of molybdenum.

4. Discussion

4.1. Phase stability analysis

A calculated temperature dependences of phase fractions diagram is shown in Fig. 16 to evaluate the phase stability of GH984G by the J-MatPro program [39]. The results predict that the primary precipitates are γ'. The γ' phase plays a large role in providing corrosion resistance, and the effect of the γ' phase on the corrosion resistance is positively related to its fraction. The γ' phase decreases with an increasing temperature due to coarsening, which is consistent with results described in the literature [15,16]. The σ phase fraction also decreases with an increasing temperature and disappears at 726 °C. The σ phase is undesirable due to tying up available chromium [15]. There is no undesirable η phase due to retaining an appropriate aluminium/titanium ratio [16].

4.2. Kinetics of corrosion

Since the oxidation kinetics of the tested alloys at different temperatures follow a parabolic law (Wagner law), as illustrated in Fig. 3, the oxidation rate is likely controlled by the diffusion process [40]. In a diffusion-controlled process, the activation energy of oxidation (Ea) can be estimated according to the Arrhenius equation:

$$k_p = k_0 \exp(\frac{-E_a}{RT}) \quad (2)$$

where T is the temperature, k_0 is the pre-exponential factor, and R is the gas constant (8.314 J mol^{-1} K^{-1}). The Ea values in the range of

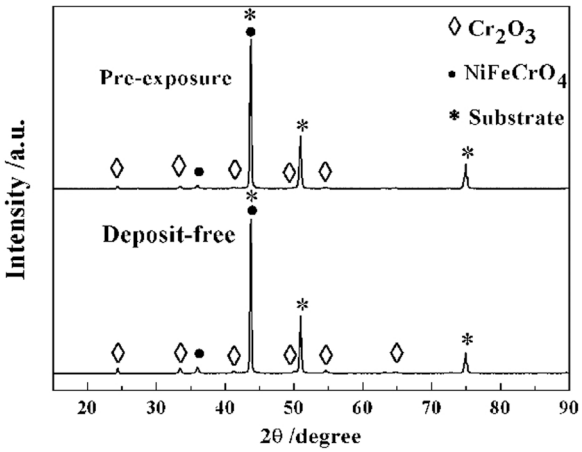

Fig. 14. XRD patterns of the surface scales on GH984G under pre-exposure and deposit-free conditions for 1000 h at 780 °C.

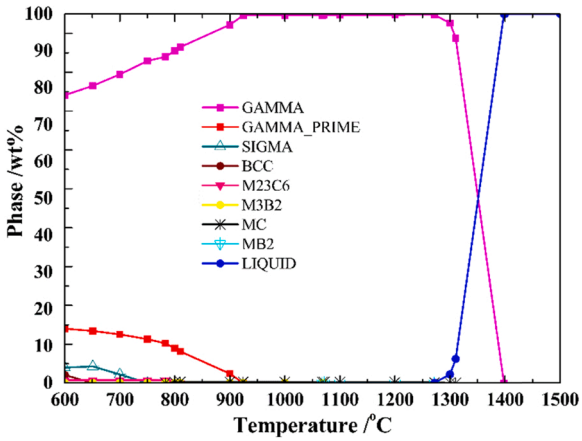

Fig. 16. Calculated phase fraction vs. temperature profiles for GH984G.

600–780 °C can be obtained from the slope of the linear fit between Inkp and 1/T and are shown in Fig. 17 and Table 4. The oxidation activation energy is related to the formation and growth of oxides and can be utilized to compare the oxidation resistance of alloys. The lower the Ea value, the more easily oxidation occurs. The Ea values of GH984G, C-HRA-1 and Alloy 625 are estimated to be 148.1, 152.1 and 137.2 kJ mol^{-1}, respectively. The Ea values of the three alloys can be ranked from large to small: C-HRA-1 >GH984G>Alloy 625. The order of the Ea values for the three alloys is negatively related to that of the oxide scale thicknesses in Fig. 4. These results indicate that the activation energy is related to the scale thickness. Clearly, the Ea values are significantly influenced by the composition of the tested alloys; thus, the role of constituent elements in the corrosion process needs to be studied.

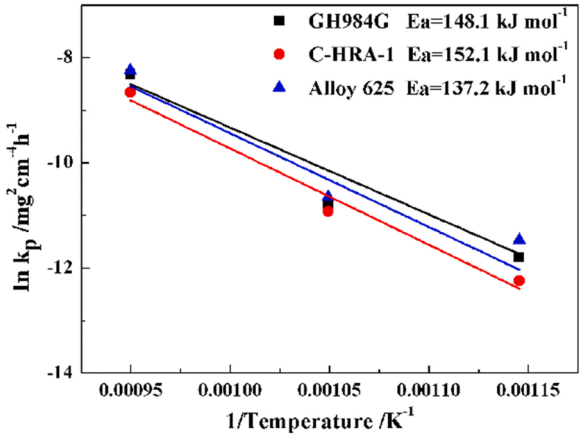

Fig. 17. Activation energies (Ea) of GH984G, C-HRA-1 and 625 in the range of 600–780 °C.

4.3. Role of constituent elements

The continuous and exclusive external Cr_2O_3 scale as a good diffusion barrier can effectively resist high-temperature corrosion [1,32,41]. A continuous Cr_2O_3 scale without spinel will restrict the inward diffusion of oxygen and sulfur due to the higher diffusion rate of oxygen and sulfur in spinel than in Cr_2O_3 [42]. A high chromium content is expected to provide better corrosion resistance because of the formation of a more

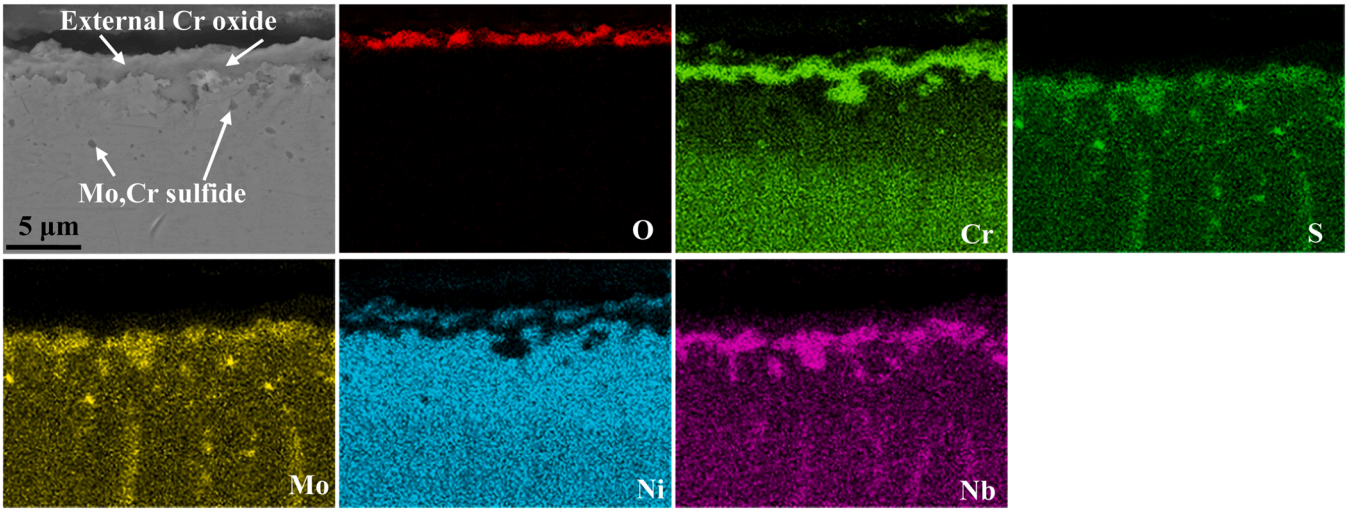

Fig. 15. EDS mapping results of the pre-exposure Alloy 625 samples after exposure for 1000 h at 780 °C.

Table 4
Activation energies (Ea) of the three alloys in the range of 600–780 °C (kJ mol^{-1}).

Material	Ea
GH984G	148.1
C-HRA-1	152.1
Alloy 625	137.2

compact and continuous Cr_2O_3 layer on the surface of austenitic alloys [40]. Gagliano et al. [38] studied the coal ash corrosion performance of 19 alloys containing 16–44% chromium and confirmed that alloys containing over 22% chromium exhibit satisfactory corrosion resistance. Thereby the critical concentration of chromium N_{Cr}, which is essential to form and maintain a continuous and exclusive external Cr_2O_3 scale can be evaluated as 0.22. In this study, the GH984G with minimum Cr content (20.9%) exhibited excellent oxidation and sulfidation resistance. It can be inferred that NCr might decrease for Ni-Fe-Cr alloys. In accordance with Wagner's diffusion theory, we can infer that the critical concentration of chromium N_{Cr} is inversely proportional to diffusion coefficient of chromium in the matrix [43,44]. The effect of introduced by Fe on the diffusion of Cr in fcc Ni lattice can be analysed by first-principles density functional theory calculations.

For vacancy-mediated solute diffusion, diffusion coefficient of a solute can be determined by Eq. (3) [45].

$$D = \upsilon_0 d^2 e^{-Q/kT} \tag{3}$$

Where υ_0 is the atom vibrational frequency; and d is the lattice constants; k and T are the Boltzmann's constant and the temperature; Q is the diffusion activation energy, and can be expressed by Eq. (4) [45].

$$Q = E_f^{vac} + E_m \tag{4}$$

Where Em is the migration energy, and E_f^{vac} is the vacancy formation energy. The equation used to calculate E_f^{vac} is given in Eq. (5) [46].

$$E_f^{vac} = E_{vac} - (N-1)E_{tot}/N \tag{5}$$

Where $E_{tot}(N)$ is the total energy of the supercell with N atoms with no vacancy, E_{vac} is the energy of the supercell with a monovacancy.

In fcc Ni lattice, the vacancy-mediated solute diffusion includes two processes: vacancy formation and hopping of Cr atom to its adjacent vacancy [47]. In accordance with transition state theory, the migration energy was calculated by the supercell energy difference between Cr atom at the saddle point and the initial position, using linear and quadratic synchronous transit (LST/QST) methods.

In order to highlight the influence of Fe addition on the diffusion of Cr atom in fcc Ni matrix, a substitutional Fe atom is located at the nearest-neighbor site of Cr atom. For Cr atom diffusion, we consider the hopping mode of Cr atom to its adjacent vacancy: Cr atom jumps to the vacancy nearest-neighbor position of Fe atom along < 110 > direction.

The vacancy formation energies, the migration energies and the diffusion activation energies in the cases of with and without Fe atom in fcc Ni matrix were calculated, and shown in Table 5. The calculated E_f^{vac} and E_m is 1.524 eV and 1.523 eV, respectively, in the case of a single Cr atom without an accompanying Fe atom in fcc Ni matrix, in agreement with other ab initio results by Janotti [47]. With the presence of Fe atom, E_f^{vac} and E_m is 1.601 eV and 1.231 eV, respectively. Finally, the above calculated results yield Q of 3.047 eV and 2.832 eV in without and with Fe atom in Ni matrix according to the sum of E_f^{vac} and E_m. Therefore, it is expected that introduction of Fe decreases the diffusion activation energy of Cr in Ni lattice. According to Eq. (3), reduction in diffusion activation energy benefits increase of diffusion coefficient of Cr in the matrix.

Table 5
The calculated energetics for vacancy-Cr diffusion in fcc Ni matrix with and without Fe atom (eV).

	E_f^{vac}	E_m	Q
Cr	1.524	1.523	3.047
Cr-Fe	1.601	1.231	2.832

The beneficial effect of the iron addition on the formation of external chromia scale was confirmed with experimental results by Xie and Zhang [48,49]. Therefore, the evaluated value of N_{Cr} (0.22) might decrease for Ni-Fe-Cr alloys. The formation and maintenance of the protective external Cr_2O_3 scale of GH984G with 20.9% Cr (<22% Cr) can be explained by the addition of 20.71% iron.

However, the Ni-Fe-Cr-based superalloys containing excess iron (more than 30%) form multi-oxide external scales on top, as reported in the literature [9,11,12], which might be explained by excessive depletion of chromium due to selective oxidation. Ni-20Cr alloyed with 0–15% Fe alloys exposed to dry CO_2 gas at 800 °C also do not form a protective chromia scale [49]. Therefore, an appropriate content of iron and chromium is responsible for the development and maintenance of an effective protective external Cr_2O_3 scale. However, Alloy 718 (Ni-19Fe-19Cr-3Mo-5 Nb+0.5Al+0.9Ti), wt%) containing chromium and iron contents similar to those of GH984G forms a three-layered scale consisting of a multi-oxide external oxidation layer, an internal sulfide layer and an intermediate layer after exposure to U.S. Eastern coal ash deposits at 750 °C [50], which indicates that the protective Cr_2O_3 scale is influenced by other critical constituent elements.

Proportionate contents of aluminium and titanium are proposed to contribute to the formation of chromia scales with appropriate thicknesses. The role of aluminium and titanium in corrosion resistance in similar environments has been discussed in several studies [32,33,41]. The outward diffusion rate of titanium is apparently higher than that of aluminium [32]. Therefore, aluminium forms internal oxides along high-angle grain boundaries in the matrix, and titanium oxide tends to form on the chromia scale. The formation of internal alumina can inhibit the diffusion of chromium and oxygen along the high-angle boundaries of nickel and suppress the formation of massive cavities in the oxide layer [32,51]; thus, internal alumina restricts chromium oxidation on the surface of alloys. In contrast, the oxidation of titanium can increase cavity formation and accelerate Cr_2O_3 formation; thus, oxidized titanium improves the sulfidation resistance via the formation of more chromia [41]. That is, the formation of protective Cr_2O_3 scale with an optimum thickness on the alloy surface can be attained by utilizing proportionate contents of aluminium and titanium.

4.4. Corrosion mechanism

As discussed above, the oxidation kinetics of GH984G follow the Wagner law. At the initial stage, the corrosion process is controlled by the inward diffusion of oxygen; then, nickel oxide nuclei grow rapidly, and a transient nickel oxide scale is formed [40,52]. A high iron content contributes to the formation of an abundance of iron oxides on the surface due to the significant solubility of iron in NiO [53]. Oxygen diffuses inward to the scale-matrix interface and reacts with chromium to form more stable Cr_2O_3 due to chromium having a lower oxidation activation energy than iron and nickel [33]. Moreover, the outward diffusion rate of chromium is obviously higher than the inward diffusion rate of oxygen within the Cr_2O_3 scale [54], which allows chromium to eventually diffuse to the oxide/oxygen interface and react with oxygen. The oxidation process enters the next stage after the oxide scale reaches a certain thickness. At this stage, the oxidation process is determined by the diffusion of ions through the oxide scale. Since the addition of iron can improve Cr_2O_3 formation, the formation of more Cr_2O_3 restricts the inward and outward diffusion of active ions and further inhibits the oxidation of nickel and iron. The small amount of oxygen that diffuses inward through the Cr_2O_3 scale bonds with aluminium due to aluminium having a significantly higher affinity towards oxygen than

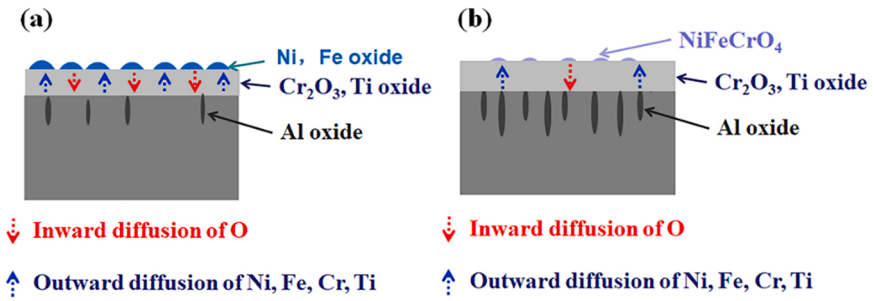

Fig. 18. Schematic showing the evolution of the oxide scale of GH984G after 168 h (a) and 1000 h (b).

the other constituent elements. This result is well evidenced by the disappearance of iron and nickel after 1000 h of exposure, as observed for GH984G in steam at 700 °C by Wang and co-workers [17]. The whole evolution of the oxidation process is illustrated in Fig. 18. Eventually, the Cr_2O_3 layer with an optimum thickness that can effectively resist oxidation and sulfidation is developed and maintained by having proportionate contents of aluminium and titanium.

5. Conclusions

The gas-phase and coal ash-related fireside corrosion behaviours of GH984G and two other contrast alloys have been investigated. Conclusions can be drawn as follows:

All tested alloys exhibited satisfactory oxidation resistance. The oxidation kinetics of the tested alloys followed the Wagner law under deposit-free conditions. The oxidation activation energy of the three alloys at 600–780 °C could be ranked from large to small: C-HRA-1 >GH984G>Alloy 625. Corrosion rates increased with an increasing temperature in the range of 600–780 °C under deposit-free conditions. GH984G and C-HRA-1 both exhibited excellent oxidation and sulfidation resistance under pre-exposure conditions, while Alloy 625 showed much less sulfidation resistance than the others due to the presence of molybdenum.

A high chromium content was expected to provide better corrosion resistance because of the formation of a more compact and continuous Cr_2O_3 layer. The moderate increase in iron for GH984G displayed a beneficial influence on the formation of the protective external Cr_2O_3 scale. Therefore, superior processing properties and cost-effective candidate alloys for A-USC could be designed by utilizing an appropriate addition of iron to the alloy in the future. Moreover, proportionate contents of aluminium and titanium contributed to the development and maintenance of the protective Cr_2O_3 scale with an optimum thickness.

CRediT authorship contribution statement

Jiali Wang: Investigation, Methodology, Formal analysis, Writing – original draft. **Jiankun Zhuo:** Project administration, Supervision, Writing – review & editing. **Qiang Yao:** Resources, Conceptualization, Supervision.

Data Availability

The raw/processed data required to reproduce these findings cannot be shared at this time as the data also forms part of an ongoing study.

Acknowledgements

This work was supported by the National Key Research and Development Program of China (2019YFE0100100). The authors are also grateful to U.S.-China Clean Energy Research Center-Advanced Coal Technologies Consortium (CERC-ACTC).

Conflict of interest statement

We declare that we have no financial interests or personal relationships that can have appeared to influence the work reported in this manuscript “Investigation of the fireside corrosion of a new wrought Ni-Fe-Cr-based alloy in advanced ultra-supercritical steam boilers”.

References

[1] R. Purgert, J. Shingledecker, R. Ganta, J. Pschirer, P. Weitzel, Sarver J., B. Vitalis, Final technical report: Boiler materials for ultra-supercritical coal powerplants, DOE Award Number: DE-FG26–01NT41175, ODSA-OCDO Grant Number: D-05–02 (A), 2015.
[2] Z. Liu, Status of the power industry in China and overall progress for A-USC technology, In: Proceedings of EPRI 8th International Conference of Advances in materials Technology for Fossil Power Plants, 2016.
[3] R. Viswanathan, J.F. Henry, J. Tanzosh, G. Stanko, J. Shingledecker, B. Vitalis, R. Purgert, U.S. program on materials technology for ultra-supercritical coal power plants, J. Mater. Eng. Perform. 14 (2005) 281–292.
[4] R. Viswanathan, W. Bakker, Materials for ultrasupercritical coal power plants boiler materials, Part 1, J. Mater. Eng. Perform. 10 (2001) 81–95.
[5] M. Fujimitsu, History of power plants and progress in heat resistant steels, ISIJ Int. 41 (2001) 612–625.
[6] Y. Fukuda, M. Shimizu, Hot corrosion and steam oxidation properties of new heat resistant steels for ultra super critical boilers, Mater. Sci. Forum 522 (2006) 189–196.
[7] S.Q. Zhao, X.S. Xie, G.D. Smith, S.J. Patel, Research and improvement on structure stability and corrosion resistance of nickel-base superalloy Inconel740, Mater. Des. 27 (2006) 1120–1127.
[8] A.G. Mohammad, M. Mohsen, Effect of long-term service exposure on microstructure and mechanical properties of Alloy 617, Mater. Des. 35 (2011) 2695–2700.
[9] Z.H. Zhong, Y.F. Gu, Y. Yuan, Z. Shi, A new wrought Ni–Fe-base superalloy for advanced ultra-supercritical power plant applications beyond 700°C, Mater. Lett. 109 (2013) 38–41.
[10] J.P. Shingledecker, N.D. Evans, Creep-rupture performance of $0.^{07}C$–^{23}Cr-45Ni-6W-Ti-Nb austenitic alloy (HR6W) tubes, Int. J. Pres. Ves. Pip. 87 (2010) 345–350.
[11] Y.X. Xu, J.T. Lu, W.Y. Li, Z. Y, Y.Y. Dang, X.W. Yang, Effect and role of alloyed yttrium on the fireside corrosion behaviour of Ni-Fe based alloys for 750°C ultra-supercritical boiler applications, Corros. Sci. 143 (2018) 148–156.
[12] Z. Yang, J.T. Lu, Z. Yang, Y. Li, Y. Yuan, Y.F. Gu, Oxidation behavior of a new wrought Ni-30Fe-20Cr based alloy at 750°C in pure steam and the effects of alloyed yttrium, Corros. Sci. 125 (2017) 106–113.
[13] C.S. Wang, Y.A. Guo, J.T. Guo, L.Z. Zhou, Investigation and improvement on structural stability and stress rupture properties of a Ni-Fe based alloy, Mater. Des. 88 (2015) 790–798.
[14] T.T. Wang, C.S. Wang, J.T.Guo, L.Z.Zhou, Stability of microstructure and mechanical properties of GH984G alloy during long-term thermal exposure, In: 19th Chinese materials conference, 2012.
[15] M.L. Tan, C.S. Wang, Y.A. Guo, Influence of Ti/Al ratios on γ′ coarsening behavior and tensile properties of GH984G alloy during long-term thermal exposure, Acta Metall. Sin. 50 (2014) 1260–1268.
[16] T.T. Wang, C.S. Wang, W. Sun, X.Z. Qin, J.T. Guo, L.Z. Zhou, Microstructure evolution and mechanical properties of GH984G alloy with different Ti/Al ratios during long-term thermal exposure, Mater. Des. 62 (2014) 225–232.
[17] C.S. Wang, L.L. Guo, L.Y. Tang, R.C. Zhou, J.T. Guo, L.Z. Zhou, Oxidation behavior of GH984G Alloy in steam at 700°C, Acta Metall. Sin. 55 (2019) 893–901.
[18] (a) N. Otsuka, Fireside corrosion of austenitic tube materials for advanced USC boilers, Mater. Sci. Forum 696 (2011) 206–211;
(b) C. Cain, W. Nelson, Corrosion of superheaters and reheaters of pulverized-coal-fire boiler. II, J. Eng. Gas Turbines Power 83 (1961) 194–201.
[19] G.M. Liu, H.C. Yang, Q. Liang, X.C. Yang, S.P. Ren, J.H. huang, Corrosion behavior of the Ni-Cr-Fe base superalloy GH984G in a synthetic coal ash and flue gas environment, Acta Metall. Sin. 30 (2017) 863–868.

[20] G.M. Liu, S.P. Ren, Q. Liang, H.C. Yang, C.S. Wang, L.Z. Zhou, High temperature corrosion behavior of superalloy GH984G in synthetic flue gases environments, 5th ICADME, 2015.
[21] P. Castello, V. Guttmann, N. Farr, G. Smith, Laboratory simulated fuel-ash corrosion of superheater tubes in coal-fired ultra-supercritical boilers, Mater. Corros. 51 (2000) 786–790.
[22] S.Q. Xu, T.T. Wang, investigation on microstructure stability of C-HRA-1 used for superheater / reheater in 700℃ advanced ultra-supercritical unit, thermal power generation, 45 (2016) 64–69.
[23] Z.G. Lu, S.Z. Qu, L. Chen, Study on long term performance of C-HRA-1 nickel base alloy welded joints at elevated temperatures, Boil. Technol. 48 (2017) 42–46.
[24] Corrosion of metals and alloys-method for metallographic examination of samples after exposure to high temperature corrosive environments, Draft ISO standard, ISO/TC 156 NWI 5092005, 2006.
[25] W.T. Reid, External Corrosion and Deposits, Elsevier, New York, 1971.
[26] I.G. Wright, C.W. Price, R.B. Herchenroeder, Electric Power Research Institute report EPRI-FP-557, Palo Alto, CA, 1978.
[27] S.J. Clark, M.D. Segall, C.J. Pickard, P.J. Hasnip, M.I.J. Probert, K. Refson, First principles methods using CASTEP, Z. Krist. 220 (2005) 567–670.
[28] J.P. Perdew, K. Burke, M. Ernzerhof, Generalized gradient approximation made simple, Phys. Rev. Lett. 77 (1996) 3865–3868.
[29] J.J. deBarbadillo, B.A. Baker, R.D. Gollihue, S.J. Patel, Alloy 740H component manufacturing development, in: Proceedings: Energy Materials Conference, CSM and TMS, Wiley Press, Xi'an China, 2014, 203–210.
[30] M.P. Agustianingrum, U. Lee, N. Park, High-temperature oxidation behaviour of CoCrNi medium-entropy alloy, Corros. Sci. 173 (2020), 108755.
[31] G.A. El-Awadi, S. Abdel-Samad, E.S. Elshazly, Hot corrosion behavior of Ni based Inconel 617 and Inconel 738 superalloys, Appl. Surf. Sci. 378 (2016) 224–230.
[32] M. Abbasi, D.I. Kim, J.H. Shim, W.S. Jung, Effects of alloyed aluminum and titanium on the oxidation behavior of INCONEL 740 superalloy, J. Alloy. Compd. 658 (2016) 210–221.
[33] F.H. Stott, G.C. Wood, J. Stringer, The Influence of alloying elements on the development and maintenance of protective scales, Oxid. Met. 44 (1995) 113–145.
[34] G.D. Li, S.Q. Li, Q. Huang, Q. Yao, Fine particulate formation and ash deposition during pulverized coal combustion of high-sodium lignite in a down-fired furnace, Fuel 143 (2015) 430–437.
[35] N.N. Aung, X.B. Liu, Effect of temperature on coal ash hot corrosion resistance of Inconel 740 superalloy, Corros. Sci. 82 (2014) 227–238.
[36] G. Stein-Brzozowska, R. Norling, P. Viklund, J. Maier, G. Scheffknecht, Fireside corrosion during oxyfuel combustion considering various SO_2 contents, Energy Procedia 51 (2014) 135–147.
[37] L. Brewer, R. Lamoreaux, The Mo-S system (Molybdenum–Sulfur), Bull. Alloy Phase Diagr. 1 (1980) 93–95.
[38] M. Gagliano, H. Hack, G. Stanko, Update on the fireside corrosion resistance of proposed advanced ultra-supercritical superheater and reheater materials: laboratory and field test results. In: The 34th clear conference on coal utilization and fuel systems, clearwater, FL, USA, 2009.
[39] Phase stability data comes from J-MatPro the materials property simulation software.
[40] (a) Y.O. Choi, J.W. Han, H.S. Hong, H.G. Suk, Study on the corrosion resistance of high strength bolt, nut and washer set (S10T) related to the surface treatment conditions, J. Weld. Join. 36 (2018) 34–39;
(b) G.C. Wood, High-temperature oxidation of alloys, Oxid. Met. 2 (1970) 11–57.
[41] G. Stein-Brzozowska, D.M. Flórez, J. Maier, G. Scheffknecht, Nickel-base superalloys for ultra-supercritical coal-fired power plants: fireside corrosion. Laboratory studies and power plant exposures, Fuel 108 (2013) 521–533.
[42] Z. Zeng, K. Natesan, Z. Cai, D. Gosztola, R. Cook, J. Hiller, Effect of element diffusion through metallic networks during oxidation of Type 321 stainless steel, J. Mater. Eng. Perform. 23 (2014) 1247–1262.
[43] C. Wagner, Reaktionstypen bei der oxydation von legierungen, Z. Elektrochem. 63 (1959) 772–782.
[44] C. Wagner, Theoretical analysis of the diffusion processes determining the oxidation rate of alloys, J. Electrochem. Soc. 99 (1952) 369–380.
[45] M. Krčmar, C.L. Fu, A. Janotti, R.C. Reed, Diffusion rates of 3d transition metal solutes in nickel by first-principles calculations, Acta Met. 53 (2005) 2369–2376.
[46] X.Y. Gao, H.P. Ren, C.L. Li, H.Y. Wang, H.J. Tan, First-principles study of the effect of lanthanum on the niobium diffusion in fcc Fe, Int. J. Mod. Phys. B 30 (23) (2016) 1650157–1–1650157–8, 1650157-1-8.
[47] A. Janotti, M. Krčmar, C.L. Fu, R.C. Reed, Solute diffusion in metals: larger atoms can move faster, Phys. Rev. Lett. 92 (8) (2004) 085901-1–085901-4, 085901-1-4.
[48] Y. Xie, T. Liang, J.Q. Zhang, D.J. Young, W.S. Zheng, Effect of Fe on corrosion of Ni-20Cr and Ni-30Cr alloys in wet CO_2 gas at 650 and 700°C, Corros. Sci. 154 (2019) 129–143.
[49] Y. Xie, T. Liang, J.Q. Zhang, D.J. Young, Effects of Fe on oxidation of Ni-20Cr and Ni-30Cr alloys at 800 °C in dry CO_2 gas, Corros. Sci. 173 (2020), 108777.
[50] Z. Zeng, K. Natesan, Z. Cai, D.L. Rink, Effect of coal ash on the performance of alloys in simulated oxy-fuel environments, Fuel 117 (2014) 133–145.
[51] F. Abe, H. Araki, H. Yoshida, M. Okada, The role of aluminum and titanium on the oxidation process of a Nickel-base superalloy in steam at 800°C, Oxid. Met. 27 (1987) 21–36.
[52] H.V. Atkinson, A review of the role of short-circuit diffusion in the oxidation of nickel chromium, and nickel-chromium alloys, Oxid. Met. 24 (1985) 177–197.
[53] A.D. Dalvi, W.W. Smeltzer, A diffusion model for oxidation of nickel-iron alloys at 1000 °C, J. Electrochem. Soc. 121 (1974) 386–394.
[54] S.J. Rothman, L.J. Nowicki, G.E. Murch, Self-diffusion in austenitic Fe-Cr-Ni alloys, J. Phys. F Met. Phys. 10 (1980) 383–398.